Nuclear Inst. and Methods in Physics Research, A 914 (2019) 46–52

Contents lists available at ScienceDirect

Nuclear Inst. and Methods in Physics Research, A

journal homepage: www.elsevier.com/locate/nima

Dependency of the capture of field emitted electron on the phase velocity of a high-frequency accelerating structure

Thomas Geoffrey Lucas [a,*], Theodorous Argyopolous [b], Mark James Boland [d], Nuria Catalan-Lasheras [b], Roger Paul Rassool [a], Claudio Serpico [c], Matteo Volpi [a], Walter Wuensch [b]

[a] University of Melbourne, Parkville 3010, Australia
[b] CERN, Geneva, Switzerland
[c] Elettra-Sincrotrone Trieste S.C.p.A., Trieste, Italy
[d] University of Saskatchewan, Saskatoon, Canada

ARTICLE INFO

Keywords:
Linear accelerators
Dark current
High gradient
X-band
Compact linear collider
Radiation

ABSTRACT

Surface electric fields within high gradient linear accelerators can exceed 200 MV/m and lead to field emitted (FE) electrons entering the structure. When the accelerating field conditions permit, these FE electrons can become captured in the RF fields and be transported through the accelerating structure as a dark current. Understanding the capture and transport of these FE currents in high frequency linear accelerators, and at accelerating gradients well above the capture threshold, is important for the operation of CERN's X-band test stands and other high gradient linear accelerators. Such dark current leads to a background radiation, which dictates shielding requirements and can damage adjacent instrumentation, as well as a background current within the structure, which can affect beam diagnostics and in the most extreme cases can cause transverse kicks on bunches. The capture of field emitted electrons is described analytically in a one dimensional approximation and is then evaluated numerically for a test structure geometry. A particular focus for the analysis is how the interaction varies with phase velocity. We demonstrate how the phase velocity varies with respect to the nominal driver frequency and structure operational temperature. Measurements on the X-band test stands at CERN demonstrate that the capture increases 12%–28% for a 1 MHz increase in the driver frequency. A three dimensional RF and particle simulation found a similar order of magnitude result for a 1 MHz increase corrborating the measurements.

1. Introduction

RF accelerating structures for the Compact Linear Collider (CLIC), and other high gradient applications, will operate with surface fields in excess of 200 MV/m [1–4]. At these surface field strengths, the spontaneous emission of electrons, known as "field emission", and subsequent capture in accelerating fields results in a propagating current [5]. For high power testing and operation of accelerating structures, this propagating current determines the background radiation dose received by local instrumentation and influences the radiation shielding requirements for experiments [6]. The current which propagates along the structure also affects beam diagnostics and in extreme cases can lead to transverse kicks on bunches [7].

Nominally, the loaded accelerating gradient and operating frequency of CLIC is 100 MV/m and 11.994 GHz for a 3 TeV version where this is reduced to 75 MV/m for the 380 GeV first stage. For this frequency, the capture threshold for an electron at rest is 64 MV/m [8], and therefore well below the operational accelerating gradient. In the following paper, we investigate an observed dependency of the propagating current on the operational phase velocity of the high frequency CLIC structures. Using conditions given in [8], we investigate the effects of how small variations in the nominal RF frequency and structure temperature affect phase velocity and therefore field emission capture. Measurements of the propagating current's dependency on phase velocity were performed on CERN's X-band test stands and then corroborated through a series of simulations using the CST Microwave and Particle Studio packages [9].

2. X-band test stands at CERN

Development of high gradient normal conducting accelerating structures is important for the feasibility of next generation linear colliders [10]. In an effort to understand the operation and reproducibility of high gradient accelerating structure, CERN has commissioned three individual X-band test stands which can test structure at high power. The three test stands, named Xbox 1, Xbox 2 and Xbox 3, generate high

* Corresponding author.
E-mail address: t.lucas@student.unimelb.edu.au (T.G. Lucas).

https://doi.org/10.1016/j.nima.2018.10.166
Received 20 August 2018; Received in revised form 18 October 2018; Accepted 22 October 2018
Available online xxxx

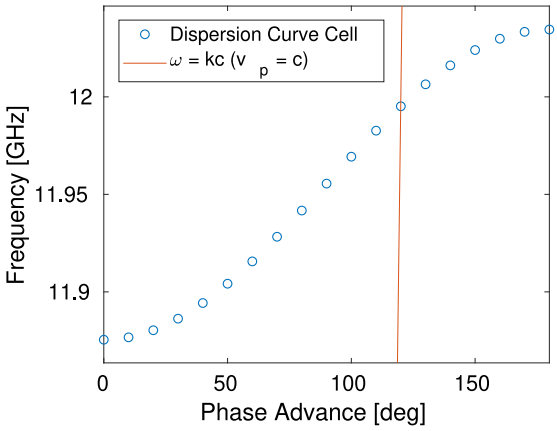

Fig. 1. Operational points on the dispersion curve for the TD26CC middle cell.

power RF pulses using X-band modulators and klystrons which operate up to 50 MW for Xboxes 1 and 2, and 6 MW which are combined to 12 MW for Xbox 3 [11–15]. After compression, using a SLED Type I RF pulse compressor, the power systems deliver above 120 MW up to 50 Hz for Xbox 1 and 2, and up to 50 MW up to 200 Hz per line for XBox 3 to the structure [12]. This high power RF produces unloaded accelerating gradients in excess of 100 MV/m, several times that seen in S-band linear accelerators, commonly used in electron linacs. Resulting from the high power RF are peak surface electric fields of approximately 200 MV/m for CLIC structures for the nominal unloaded accelerating gradient [4]. These high surface fields lead to the field emission of electrons. The emitted current density of these electrons, first described by Fowler and Nordeim in [5], is given by

$$j_F = 1.54 \times 10^{-6} 10^{4.52\phi^{-0.5}} \frac{\beta^2 E(t)^2}{\phi} \times \exp\left(-\frac{6.53 \times 10^9 \phi^{1.5}}{\beta E(t)}\right) [\mathrm{A\ m^{-2}}] \quad (1)$$

where ϕ is the work function of copper in eV, β is the field enhancement factor, and $E(t)$ is the electric field strength at the time of emission in V/m [5,16].

With such high accelerating gradients, field emitted electrons can be captured and begin to propagate along the structure known as a dark current. The condition for capture of these electrons is well known and the same as those for the electrons intended for acceleration. This condition is that the gradient is great enough such that a stationary electron can accelerate to stay synchronous with the oscillating RF field. Given a phase velocity of c, this threshold in MV/m is given by

$$E_0 \geq \frac{1.6}{\lambda} \quad (2)$$

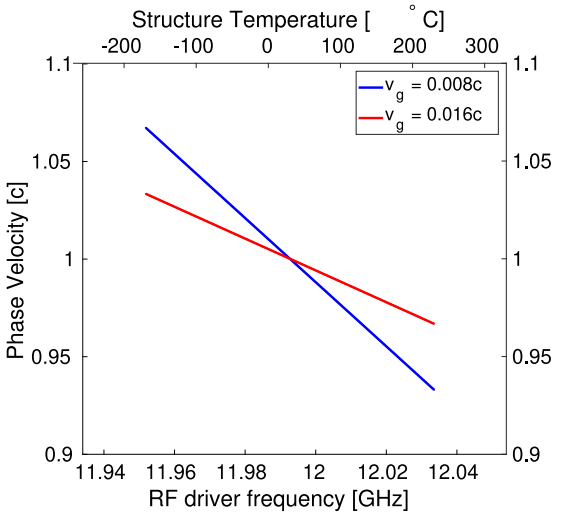

Fig. 3. Variation in the radiation due to the change in structure temperature.

where λ is the RF wavelength in metres [17]. This equation demonstrates that the capture gradient increases inversely to the RF wavelength and therefore is greater in higher frequency linear accelerators.

3. Phase velocity dependence of dark current

In Eq. (2) the threshold gradient for the capture of field emitted electrons in a linear accelerator was described for the special case of the RF phase velocity being equal to c. A more general equation for capture can be written for the case of a varying phase velocity (v_p) as

$$E_0 \geq \frac{\pi m_0 c^2}{\lambda e} \left(\frac{v_p - v_0}{v_p + v_0}\right)^{\frac{1}{2}}, \quad (3)$$

where m_0 is the mass of an electron, e is the electron charge magnitude, and v_0 is the velocity of the electrons [8]. Such a relation demonstrates that a reduction in the phase velocity reduces the required gradient for capture of low energy electrons. To understand how the phase velocity varies with the operational parameters we begin with the definitions of phase velocity and group velocity as

$$v_p = \frac{\omega}{k}, \quad (4)$$

and

$$v_g = \frac{d\omega}{dk}, \quad (5)$$

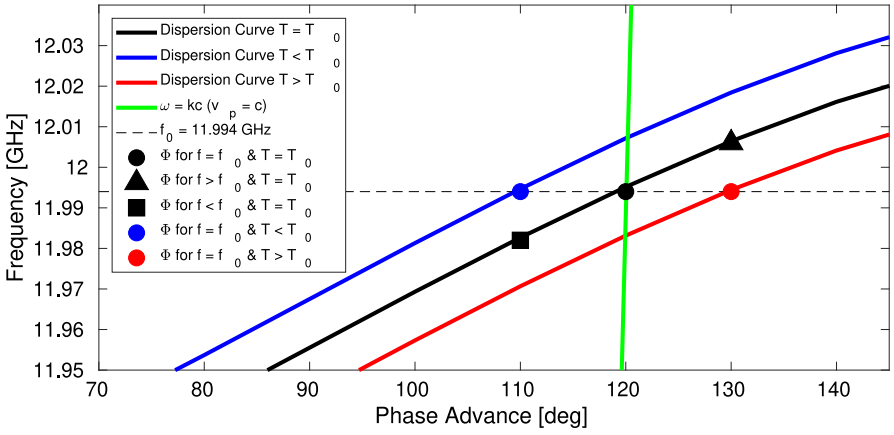

Fig. 2. Operating modes for three structure temperatures and three RF driver frequencies.

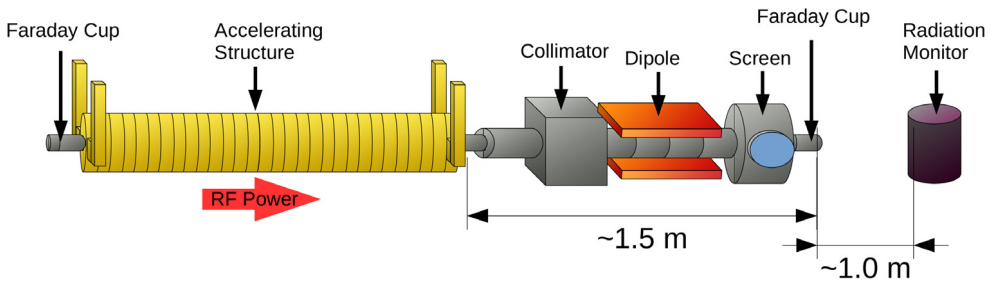

(a) Xbox 2 and spectrometer.

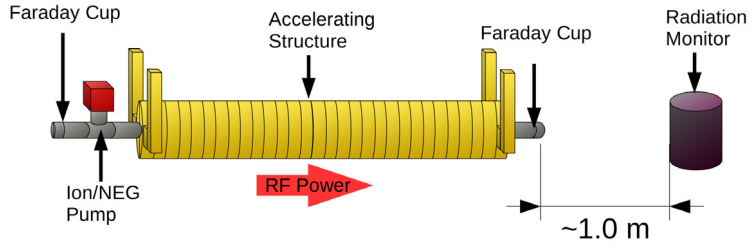

(b) Xbox 3.

Fig. 4. Experimental setup for the measurement of the dependence of dark current on the RF driver frequency and structure temperature using a radiation monitor.

respectively, where ω is the RF driver frequency and $k = 2\pi/\lambda$ is the wavenumber [17]. We see that the phase velocity can be varied through a change in ω (See Fig. 1). Differentiating Eq. (4) against ω gives the variation in phase velocity with respect to RF driver frequency as

$$\frac{dv_p}{d\omega} = \frac{1}{k} - \frac{\omega}{k^2}\frac{dk}{d\omega} \tag{6}$$

$$= \frac{1}{k}\left(1 - \frac{\omega}{k}\frac{1}{v_g}\right) \tag{7}$$

$$= \frac{\lambda}{2\pi}\left(1 - \frac{v_p}{v_g}\right). \tag{8}$$

Setting the synchronicity condition as c we find

$$dv_p = \frac{\lambda}{2\pi}\left(1 - \frac{c}{v_g}\right)d\omega. \tag{9}$$

This gives the relation between the variation in the phase velocity and driver frequency set value. From this relation we find that an increase in the driver frequency results in a decrease in the phase velocity, given typical group velocity (v_g) values for CLIC structures are well below c and given the structures are a forward travelling wave design, where the group velocity travels in the same direction as the phase velocity. For a backward travelling wave structure, the group velocity travels in the opposite direction of the phase velocity therefore an increase in the driver frequency results in an increase in the phase velocity, according to Eq. (9).

Equivalent to a variation in the RF driver frequency, a shift in the resonant frequency (ω_r) can also vary the phase velocity. Such a shift in ω_r can be achieved through a variation in the structure's operating temperature which causes thermal expansion/contraction of the structure, and therefore changes the radius of the structure's cells. The variation in the resonant frequency for a given temperature change is given as

$$\frac{d\omega_r}{dT} = -\alpha\omega_r, \tag{10}$$

where α is the thermal expansion coefficient which for copper is 17×10^{-6} K^{-1} and $\omega_r = 2\pi f_r$ is the resonant frequency ($f_r = 11.994$ GHz) in rad/s. For a 1 °C increase in the structure temperature, we see a 203 kHz decrease in f_r. In Eq. (10) we see that the change in temperature varies the resonant frequency ω_r rather the driver frequency ω. To demonstrate how $d\omega_r$ is related to $d\omega$ Fig. 2 displays the operating points for three structure temperatures and three driver frequencies. It can seen that for the phase velocity ($v_p \propto f/\phi$) an increase in the structure temperature, which Eq. (10) explains is a decrease in the resonant frequency, is equivalent to an increase in the driver frequency. From these diagrams we find that an increase in ω_r is the equal to a reduction in ω such that

$$d\omega = -d\omega_r. \tag{11}$$

Substituting Eqs. (10) and (11) into Eq. (9) we get the change in the phase velocity with respect to structure temperature change as

$$dv_p = \frac{\lambda}{2\pi}\left(1 - \frac{c}{v_g}\right)\alpha\omega_r dT. \tag{12}$$

We find that an increase in the structure temperature similarly increases the phase velocity. In Fig. 2 we plot 5 points on a dispersion curve to demonstrate Eqs. (9) and (12). At the nominal driver frequency and structure temperature (●) we see that the phase velocity is $v_p = c$ as it lies on the green line, recalling $v_p \propto \omega/\Phi$ where Φ is the phase advance per cell. For an increase in the structure temperature (●) or an increase in the driver frequency (▲) we find the operational point is below the $\omega = kc$ line and therefore $v_p < c$. Conversely, for a decrease in the structure temperature (●) or a decrease in the driver frequency (■) we find $v_p > c$.

To understand the scales required for a noticeable variation in v_p, we plot the phase velocity normalised to the speed of light against the structure temperature and driver frequency in Fig. 3 for a group velocity of $0.008c$ and $0.016c$. These group velocity values are the maximum and minimum values within the iris-tapered CLIC baseline structure design [1]. The change in the phase velocity is $0.082\%c$/MHz and $0.164\%c$/MHz for a group velocity of $0.016c$ and $0.008c$, respectively.

Table 1
RF pulse parameters for three structures under test on the two test stands.

Test stand	Structure	Power [MW]	Gradient [MV/m]	Pulse Length [ns]	Rep. Rate [Hz]
Xbox 2	TD26CC R05	43	100	170	50
Xbox 3	TD24 R05 SiC	17	64	50	50
Xbox 3	T24 PSI	33	94	200	50

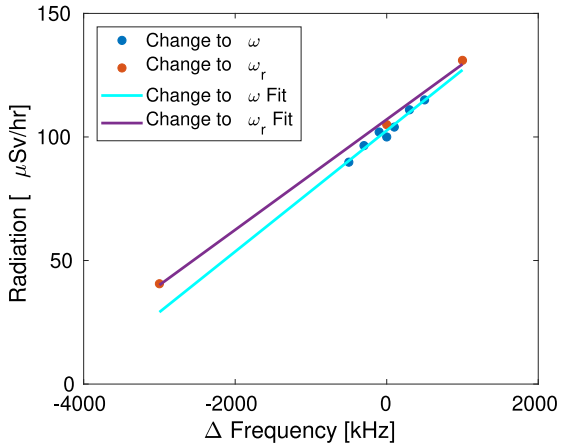

(a) TD26CC R05 N3

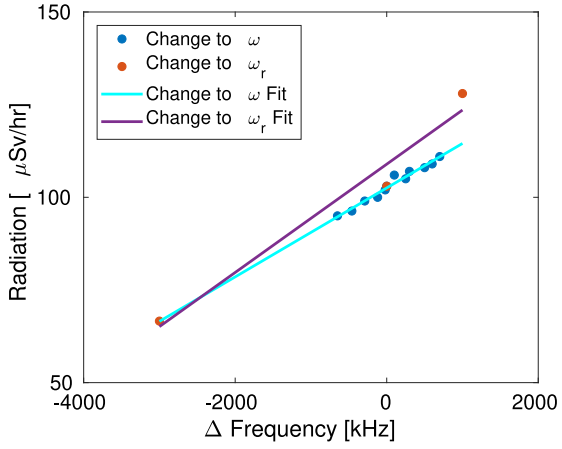

(b) T24 PSI

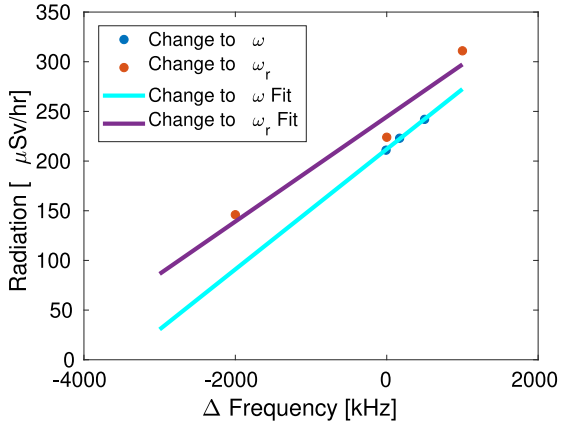

(c) TD24 R05 SiC

Fig. 5. Change in Radiation measured inside the bunker vs the change in the structure temperature and driver frequency.

Recalling Eq. (3) we saw that a decrease in the phase velocity reduces the required gradient for the capture of field emitted electrons. In summary we can state that: *The capture likelihood of field emitted electrons will increase when there is an increase in driver frequency or an increase in structure temperature due to a reduction in phase velocity, and vice versa.*

4. Measurements of dark current capture changes with phase velocity

First observations of a notable variation in the dark current level occurred by chance due to a malfunctioning structure temperature regulating chiller, during the conditioning of a test structure made from halves [18]. The incident led to a radiation safety threshold being exceeded and tripping an interlock. During this time it found that there was a strong correlation between the structure temperature and radiation outside the bunker. Testing of the dark current capture dependence on the phase velocity was performed on CERN's X-band test stands and came at a later date using three accelerating structures that were under high power testing at the time.

The RF driver frequency and structure temperature were varied for a constant peak power, pulse length and pulse repetition rate to measure the variation of steady state dark current [6]. Table 1 depicts the RF pulse parameters used for the testing on the three structures. The experimental setup of the dark current measurements for the structures installed on Xbox 2 and Xbox 3 are illustrated in Figs. 4a and 4b, respectively. The dark current measurements were performed indirectly using an ionisation chamber radiation monitor which tracked the radiation dosage at the end of the structure, known to be caused by dark current incident with the Faraday cup [6]. Between the measurements of each structure, the radiation monitor was aligned to be directly downstream of the structure under test and approximately 1 m from the end of the beamline. The spectrometer set up on Xbox 2 had its collimator and screen completely retracted during the measurement [19]. The choice of using the radiation monitor to measure dark current was due a poorly aligned Faraday cup in Xbox 2, after the spectrometer, consequently leading to poor signal strength. We will refer to the change in structure temperature as a shift in resonant frequency from here onwards, and calculate the equivalent frequency shift using Eq. (10). This will allow an easy comparison for the two operational parameter changes. Radiation measurements were performed at structure resonant frequency shifts of −3 MHz (−2 MHz for TD24 R05 SiC), 0 MHz, and +1 MHz. Likewise, radiation measurements were performed for a variation in the klystron driver frequency. Such variations in the driver frequency were restricted to ±1 MHz due to the bandwidth limitation of the klystron. In Fig. 5 we plot these radiation measurements for a given RF driver or resonant frequency shift, and fit each with a linear regression. For an increase in the RF driver and equal magnitude decrease in resonant frequency (structure temperature increase), we see an increase in the radiation level within the bunker. The vertical offset between the temperature and frequency measurements resulted from RF breakdowns causing new baseline dark current levels. When taking the driver frequency (ω) fit values we see that a 24.5%/MHz, 28.67%/MHz, and 12.64%/MHz shift in the radiation levels for the TD26CC, TD24SiC, and T24PSI, respectively. This increase in dark current for an increase in driver frequency and decrease in resonant frequency (increase in structure temperature) is what is expected from Eqs. (9) and (12) supporting the change in phase velocity as the mechanism for the dark current variation.

5. A three-dimensional simulation of dark current capture changes with phase velocity

To further study the effects of phase advance on field emitted current capture simulation have been made using CST Microwave and Particle Studio [9]. Calculating the entire structure geometry for RF fields and particle simulations required too much computation power to make it feasible. Instead, to obtain the electric and magnetic field distributions, we began with the eigenmode solver and a single cell geometry. The middle cell from the TD26CC R05 structure, currently the CLIC baseline structure, was used for the single cell geometry [4]. In this cell, the iris radius is 2.75 mm resulting in a group velocity of around $0.012c$. For the boundary conditions we started with $\Phi = 2\pi/3$ (120°) mode, as

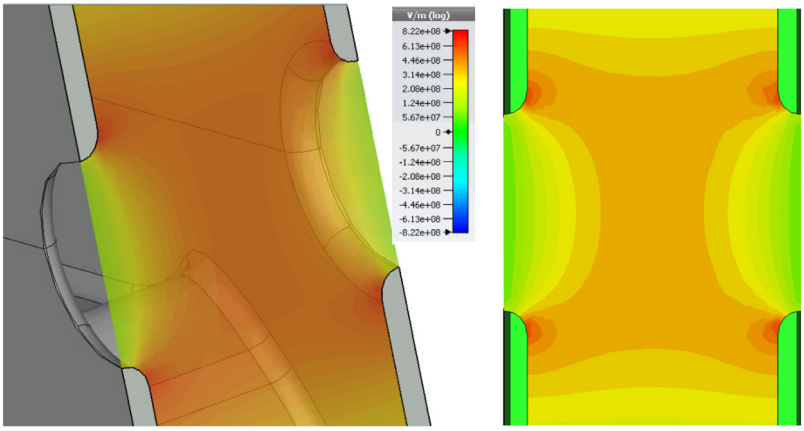

Fig. 6. Eigenmode Solution for the TD26CC R05 cell.

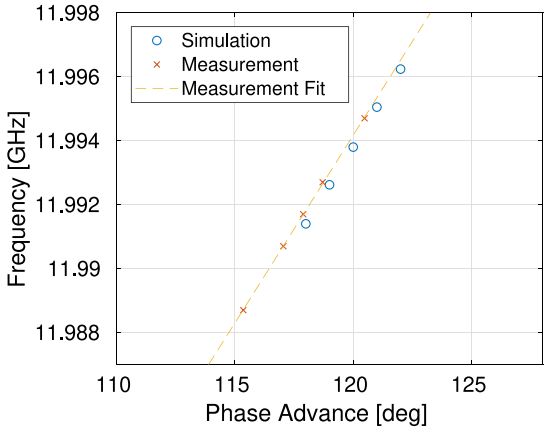

Fig. 7. Dispersion curve for the eigenmode solutions from the RF simulation overlaid on the RF measurements.

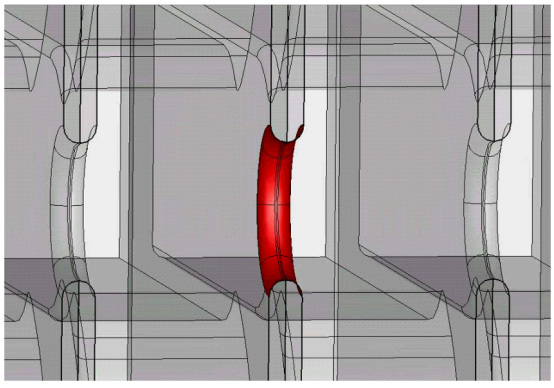

Fig. 8. Iris emission area used in the PIC solver.

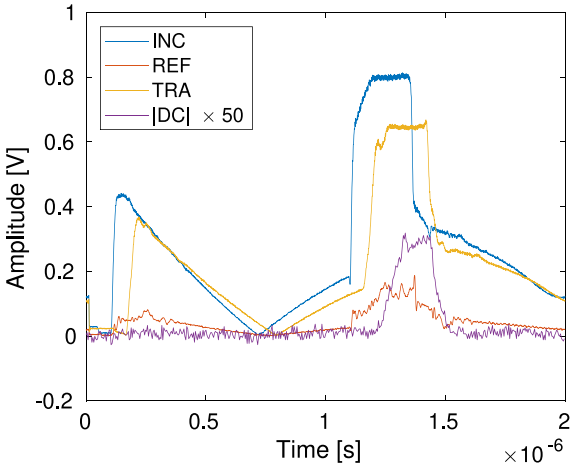

Fig. 9. Sample incoming (INC), reflected (REF), and transmitted (TRA) RF waveforms along with the downstream Faraday cup signal (DC).

used in the CLIC design, then solved the E and H fields for a single cell (Fig. 6). Surface electric fields are seen to be greatest near the iris and therefore are expected to be main source of field emitted electrons [5]. Running the eigenmode solver for various Φ values allowed a change in the frequency of the cell. In Fig. 7, the five points on the dispersion curve are plotted for different Φ values on the single cell geometry. The phase and group velocity is found using Eqs. (4) and (5), setting $k = \Phi/L_{cell}$ where L_{cell} is the cell length. These give the phase velocity and group velocity as $v_p = c$ and $v_g = 0.011998c$, respectively, which agrees well with the expected value. A non-perturbative bead-pull measurement gave the electromagnetic field distributions along the structure which demonstrated good agreement with the simulation [20,21].

For the particle model, a 48 cell model was assembled to understand the upstream and downstream behaviour of a 24 cell structure [7]. From Floquet's Theorem, we find that for infinitely repeating coupled cells electromagnetic fields in each cell differ by only a phase difference [8]. Based on this, the single cell electromagnetic fields were imported into each of the adjacent cells with the appropriate phase advance for the given RF driver frequency (119° for 11.9926 GHz, 120° for 11.9938 GHz, and 121° for 11.995 GHz). Using the single cell geometry and its electromagnetic field solutions for each of the 48 cells allows the structure to act as a constant gradient structure, although the structure lacks the iris tapering seen in the structures under test. This simplified geometry was used to reduce the computational time of the simulation.

Two dimensional monitors at each iris measured the properties of particles emitted from the centre of the 48 cells. The idea of using this symmetry for upstream and downstream behaviour of a full structure model was exploited in [7]. As the source of the particle, we set the iris as the emission area where the fields are greatest (Fig. 8) and therefore the field emitted current density is greatest. To find the density of field emitted electrons, the emission area used the Fowler–Nordheim model described in Eq. (1). By setting the total area of the iris as the emitter, early simulations found that the downstream current is well beyond that measured. Emitters in structures are known to be microscopic in nature and therefore their area vastly smaller than the area of the iris [16]. For the model we add an emitter density factor to determine the effective area of the emitter(s). Measurements in X-band test stands

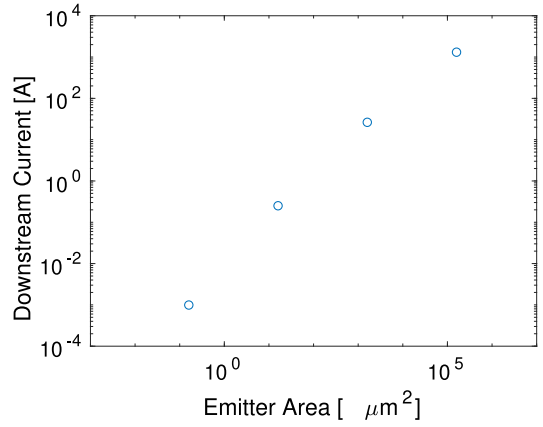

Fig. 10. Scan of the effective area of emission for the iris.

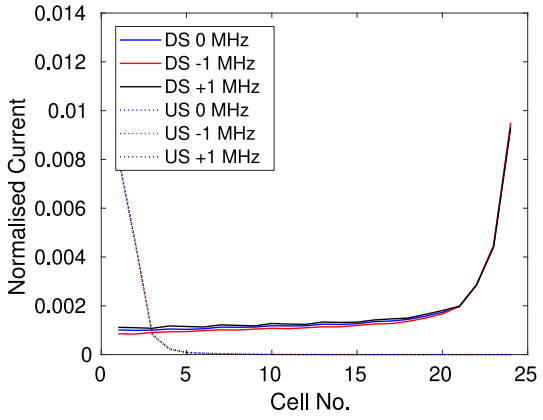

(a) Per Cell

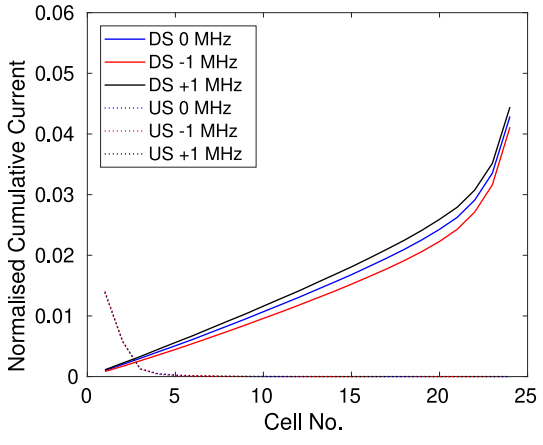

(b) Cumulative

Fig. 11. Results of dark current capture for PIC simulation.

at CERN demonstrate downstream currents in the hundreds of microamp to milliamp regime (Fig. 9). Fig. 10 plots the downstream current against the effective area of the emitter and shows that the effective area size is from 0.01 to 1 μm^2. We take the upper limit of the emitter size and spread the effective emitter area homogeneously across the entire iris as it is yet known how the emitter's position on the iris affects the capture of dark current. The scaled emission current density (j'_F) used for the final simulation is given by multiplying the current density (j_F) by the ratio of the effective emitter area to the iris area such that

$$j'_F = \frac{A_{emitter}}{A_{iris}} j_F, \tag{13}$$

where $A_{emitter}$ is the effective area of the emitter and A_{iris} is the area of the iris. In the emission model we chose a field enhancement factor β of 30, a typical value measured in experiments, and the work function for copper to be 4.5 eV [22].

6. Simulation results

To investigate the changes in captured dark current, Fig. 11 displays the capture efficiency from each cell. Plotting the capture as a percentage for each cell (Fig. 11a), as well as an accumulation along the structure towards each respective output (Fig. 11b), the capture efficiency is seen to increase for a greater frequency RF driver as seen in measurements. Simulations demonstrated that particles emitted later in the RF oscillation are captured for higher driver frequencies whereas they slip from the bucket at lower driver frequencies. This effect is therefore seen for the field emitted particles which have undergone capture, which is important for our analysis of the simulations. In Figs. 6 and 8 of [7] it was shown that the low energy particles in the cells far downstream predominantly were not measured in the Faraday cups as these particles were not captured well enough for transmission through the beam pipe, housing the vacuum system, and on to the Faraday cup. These low energy particles are seen as the jump in transmission downstream in cells 21 to 24 of Fig. 11a. Taking this into account, our analysis looked at the particles arriving downstream of the structure which are known to have been captured (cells 1 to 20), and therefore likely to arrive at the Faraday cup due to their lower emittance and greater longitudinal momentum. From cells 1 to 20, the cumulative capture for the nominal driver frequency is 0.0243 compared to 0.0259 for +1 MHz and 0.0223 for −1 MHz. This accounts for an average of 8.05%/MHz change in the capture of the dark currents with respect to the driver frequency change for 20 cells. In Fig. 12 we compare these simulation results to the measurement results from Fig. 5 where we use the change in driver frequency. We find a similar magnitude change in the dark current between the simulation and measured results for the T24 PSI structure. The large difference between the T24 PSI structure and the other two structures is yet to be understood and will be studied in future investigations. It is expected by the authors that the difference may be caused by the location of the emitter on the iris.

7. Conclusion

X-band test stands operating at CERN operate with surface fields in excess of 200 MV/m leading to the emission and capture of field emitted electrons. A simplified one dimensional model demonstrated that the capture of these field emitted electrons was dependent on the driver frequency as well as the structure temperature, which shifted the structure's resonant frequency. This dependence was explained to be the result of a shift in the phase velocity of the RF fields. Measurements of the dependency on the X-band test stands at CERN demonstrated a strong variation in the measured dark current for a small variation in the driver frequency. Simulations of the capture of dark current also found this dependency and obtained similar variations in the capture likelihood as the measurements performed.

Acknowledgements

The authors would sincerely like to acknowledge the help of the radiation protection group at CERN for their assistance during these measurements. We would also like to thank Thibaut Lefevre and Andrea Latina for their support and input.

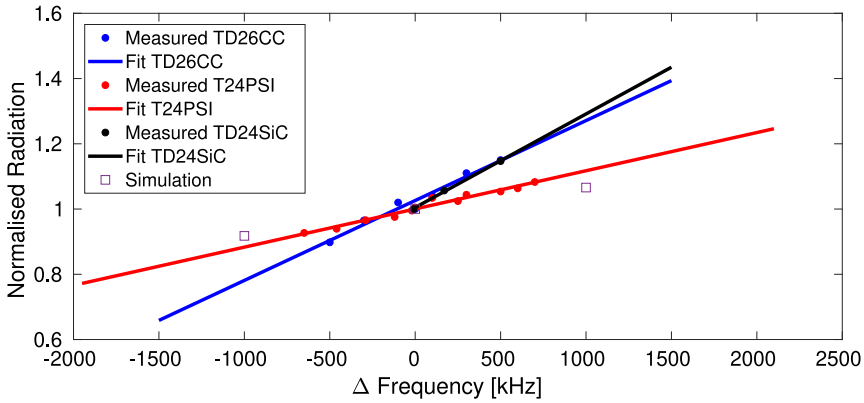

Fig. 12. A comparison of the simulated and measured radiation within the bunker for the three structure seen in Fig. 5 and normalised to the radiation measured at the nominal frequency.

References

[1] M. Aicheler, et al., A Multi-TeV Linear Collider Based on CLIC Technology, CERN 2012-007.

[2] S. Benedetti, A. Grudiev, A. Latina, High gradient linac for proton therapy, Phys. Rev. Accel. Beams 20 (2017) 040101.

[3] S. Benedetti, et al., Fabrication and testing of a novel S-Band backward travelling wave accelerating structure for proton therapy linacs, in: 28th Linear Accelerator Conference, East Lansing.

[4] A. Grudiev, W. Wuensch, Design of an X-band Accelerating STructure for the CLIC main Linac, in: Proceedings of LINAC08, Victoria, BC, Canada.

[5] R.H. Folwer, L. Nordheim, Electron emission in intense electric fields, Proc. R. Soc. Lond. Ser. A Math. Phys. Eng. Sci. 119 (1928) 173.

[6] N.V. Mokhov, I.L. Rakhno, N.A. Solyak, A. Sukhanov, Igor S. Tropin, Dark Current and Radiation Shielding Studies For The ILC Main Linac, arXiv:1705.02363 [physics.acc-ph].

[7] Karl L. F. Bane, et al., Dark currents and their effect on the primary beam in an X-band linac PRAB, 064401, 2005.

[8] CERN Accelerator School, 1992.

[9] CST STUDIO SUITE, 2018.

[10] W. Wuensch, High Gradient X-band Technology: From TeV colliders to light sources and more, CERN courier, April 2018, volume 58 number 3.

[11] N. Catalan-Lasheras, et al., Experience Operating an X-band High-Power Test Stand at CERN. http://accelconf.web.cern.ch/accelconf/IPAC2014/papers/wepme016.pdf.

[12] B. Woolley, High Power X-band RF Test Stand Development and High Power Testing of the CLIC Crab Cavity, Lancaster University, United Kingdom, 2015.

[13] M. Volpi, et al., High Power and High Repetition Rate X-band Power Source Using Multiple Klystrons. http://ipac2018.vrws.de/papers/thpmk104.pdf.

[14] N. Cataln Lasheras, et. al., Experience Operating an X-band High-Power Test Stand at CERN, 5th International Particle Accelerator Conference, Dresden, Germany, 15 - 20 Jun 2014, 2288.

[15] N. Cataln Lasheras, et. al., Commissioning of XBox-3: A very high capacity X-band test stand, in: 28th Linear Accelerator Conference, East Lansing, Michigan, 25 - 30 Sep 2016, TUPLR047.

[16] J.W. Wang, G.A. Loew, Field Emission and RF Breakdown in High-Gradient Room-Temperature Linac Structures. SLAC-PUB-7684, 1997.

[17] Wangler, RF Linear Accelerators, Wiley, 1998.

[18] T. Argyropoulos, et al., Design, fabrication, and high-gradient testing of an X-band, traveling-wave accelerating structure milled from copper halves, Phys. Rev. Accel. Beams 21 (2018) 061001.

[19] M. Jacewicz, et al., Spectrometers for RF breakdown studies for CLIC, Nucl. Instrum. Methods Phys. Res. A 828 (2016) 63–71.

[20] C.W. Steele, A non-resonant perturbation theory, IEEE Trans. Microw. Theory Tech. 14 (2) (1966) 70–74.

[21] Rolf Wegner, RF Tuning of 12SWV18026-01CSCC (TD26 CC N3) https://edms.cern.ch/document/1626878/1.

[22] W. Wuensch, CLIC Accelerating Structure Development Proceedings of EPAC08, Genoa, Italy.